The ALICE Inner Tracking System ⋆

F. Tosello

INFN, Sezione di Torino, V. P. Giuria 1, I-10125 Torino, Italy

for the ALICE Collaboration

Abstract

The design characteristics of the ALICE inner tracking system are presented together with the performances measured in beam tests and expected from Monte Carlo simulations

1 Introduction

ALICE (A Large Ion Collider Experiment) [1,2] is a detector designed to study nucleus–nucleus collisions at the LHC. At a c.m. energy of 5.5 TeV/nucleon, it will be possible to explore a radically new regime of matter, stepping up by a large factor in both volume and energy density compared to the nuclear interactions studied at the CERN-SPS and at RHIC. Thanks to the huge number of secondary particles produced, it will be possible to measure most of the relevant variables on an event–by–event basis. Moreover, the LHC energy and luminosity will allow the full spectroscopy of the Υ family and of D and B mesons.

ALICE is a general–purpose detector, in which most of the hadrons, leptons and photons produced in the interaction can be measured and identified. The baseline design consists of a central ($|\eta| \leq 0.9$) detector covering the full azimuth, complemented by a forward muon spectrometer ($2.4 \leq \eta \leq 4$) to study vector meson production [3], a multiplicity detector covering the forward rapidity region (up to $|\eta|$=4.5) and a zero degree calorimeter. The central detector will be embedded in the large L3 magnet which can run at a field between 0.2 T and 0.5 T, and will consist of a high–resolution Inner Tracking System (ITS)

⋆ presented at VERTEX 2000 "9^{th} International Workshop on Vertex Detectors", Sleeping Bear Dunes National Lakeshore, Michigan, U.S.A. September 2000

[4], a cylindrical time projection chamber, particle identification arrays (time of flight and ring imaging Cherenkov detectors), a transition radiation detector [5] for electron identification and a single–arm electromagnetic calorimeter.

The basic functions of the ITS are: determination of the primary vertex and of the secondary vertices necessary for the reconstruction of charm and hyperon decays, particle identification and tracking of low-momentum particles, improvement of the momentum and angle measurements of the TPC.

2 ITS design considerations

The following factors were taken into consideration for the design of the ITS.

Dimensions. The ITS inner radius has to be as close as possible to the beam pipe ($r_{\rm beam} = 3$ cm) to optimize vertex and impact parameter resolutions. The outer radius has to be large enough to ensure efficient track matching with the TPC, whose inner radius is fixed at 84 cm by the acceptable occupancy.

Acceptance. In order to analyze particle ratios, $p_{\rm T}$ spectra and particle correlations on an event–by–event basis, the ITS needs to cover a pseudorapidity region of about $|\eta| < 0.9$ for vertexes located within the interaction diamond ($2\sigma_{\rm z} = 10.6$ cm). This is wide enough to detect several thousand particles per heavy-ion collision at the currently predicted particle production multiplicity. Furthermore, it ensures a good acceptance for the decay products of large–mass, low-$p_{\rm T}$ particles. Finally, the full azimuthal coverage is necessary to efficiently reject the low–mass Dalitz decays, which generate the main combinatorial background for dielectron physics.

Particle identification. The ITS contributes to this issue by measuring the specific energy loss of the particles. To apply a truncated–mean method, a minimum of four ITS layers need an analogue readout with a wide enough dynamic range to provide unsaturated ${\rm d}E/{\rm d}x$ samples down to the minimum momentum for which the tracks have a reasonable ($> 20\%$) reconstruction probability.

Materials budget. Momentum and impact parameter resolutions for the low-$p_{\rm T}$ particles are dominated by multiple scattering effects in any existing tracking detector. However, from signal–to–noise ratio considerations, the detectors providing ${\rm d}E/{\rm d}x$ measurements must be approximately 300 μm thick. Furthermore, the detectors must slightly overlap in both the Rφ and Rz planes to avoid holes in the acceptance window. Thus, taking into account the incidence angles of the tracks, all the detectors represent 1.7% of X_0. In the approved ITS design [4], all the additional materials in the active volume (i.e. electronics, cabling, etc.) amount to 4.8% of X_0. The resulting momentum resolution is better than 2% for pion momenta between

100 MeV/c and 3 GeV/c.

Granularity and spatial precision. The system must cope with a track density of $dN_{\rm ch}/dy = 8\,000$ at η=0, which is the upper limit of the current theoretical predictions. This requires several million detector cells in each layer in order to keep the occupancy at the level of a few per cent, which is necessary for a reliable track finding. For charmed particle detection, the impact parameter resolution must be better than 100 μm in the Rφ plane and therefore the spatial resolution must be of few tens of μm, with the best precision (12 μm) for the detectors closest to the primary vertex.

Radiation levels. The ionizing radiation dose received by the detector components was calculated using Monte Carlo techniques based on HIJING [6], FLUKA [7] and GEANT3 [8] and an appropriate mixture of collisions at various impact parameters and beams. The calculated total dose during the experiment lifetime, reported in table 1, is low by the LHC standards but is still enough to require the use of radiation–tolerant designs for the front–end electronics, particularly to minimize latch–up phenomena. The expected neutron fluence does not cause significant damage to the detectors or the associated electronics.

Readout rate: The ALICE system will be used in two basically different readout configurations, operated simultaneously with two different triggers. The centrality trigger will activate the read out of the whole ALICE, at a rate of about 25 Hz. The dimuon trigger will only readout a subset of fast-readout detectors at a rate of about 1 kHz. In this second case, to reach the required invariant mass resolution, the two inner layers of the ITS have to be read out in less than 400 μs in order to provide the primary vertex position.

3 Layout of the ITS

The ITS consists of six cylindrical layers of silicon detectors based on three different technologies depending on the granularity and resolution requirements, as shown in table 1 and fig. 1. The particle densities in the four innermost layers impose the choice of detectors with true two-dimensional readout, namely the silicon pixels (SPD) and the silicon drift (SDD). Instead, at larger radii, the smaller occupancy allows to use double–sided silicon strip detectors with a small stereo angle. This technology has been preferred to the single-sided one in order to minimize the material and to exploit the correlation of the pulse heights, read out from the two sides, in recognizing the ghost hits originated by the projective readout. The pseudorapidity coverage of the SSD and SDD subsystems is $|\eta| < 0.9$, that of the first SPD layer is $|\eta| < 1.55$ to extend the acceptance of the multiplicity measurement.

The detectors and front-end electronics are held by lightweight carbon fibre

Table 1
Parameters of the ITS detector types. A module represents a single detector. The values in parenthesis refer to the outer layer of a pair. The occupancies include the contribution of the background. Radiation dose and neutron fluence are calculated for ten years of operation in p-p, Ca-Ca and Pb-Pb modes.

Parameter	Silicon Pixel	Silicon Drift	Silicon Strip
Radius (cm)	4.0 (7.0)	14.9 (23.8)	38.5 (43.6)
$\pm z$ (cm)	14.3 (14.3)	22.2 (29.7)	43.1 (43.8)
Ladders	20 (40)	14 (22)	34 (38)
Modules/ladder	4 (4)	6 (8)	22 (25)
Total number of modules	240	260	1698
Active area / module (mm^2)	12.8×69.6	70.0×75.3	73.0×40.0
Total active area (m^2)	0.07 (0.13)	0.42 (0.89)	2.09 (2.67)
Readout channels / module	40960	2×256	2×768
Total number of channels (k)	9830	133	2608
Power dissipation in barrel (W)	1000-1500	770	1100
Power dissipation end-caps (W)	—	410	1500
Cell size (μm^2)	50×425	150×294	95×40000
Total number of cells (M)	9.8	34.1	2.6
Spatial precision Rφ (μm)	12	35	15
Spatial precision z (μm)	100	23	730
Two track resolution Rφ (μm)	100	200	300
Two track resolution z (μm)	850	600	2400
Max. charged particle flux (cm^{-2})	89 (22)	7.2 (2.7)	1.0 (0.82)
Max. occupancy (%)	2.1 (0.6)	2.5 (1.0)	4.0 (3.3)
Cumulated dose (krad)	130 (39)	13 (5)	2 (2)
Neutron fluence ($10^{11} cm^{-2}$)	3.2 (3.1)	3.5 (3.3)	3.7 (3.3)

reinforced plastic (CFRP) linear structures called ladders. As an example, the 115 cm long SSD ladder of the outer layer weights 25 g and its central sagging at full load (250 g) is less than 60 μm. The outer four ITS layers are assembled onto a mechanical support made of two end-cap cones connected by a thin cylinder placed between the SSD and the SDD layers. This is to reduce the amount of material in the rather wide gap between the TPC and the ITS, where the track matching is more difficult. The cones and the cylinder are both made of sandwiches of CFRP and Rohacell$^{(TM)}$. The cones provide the

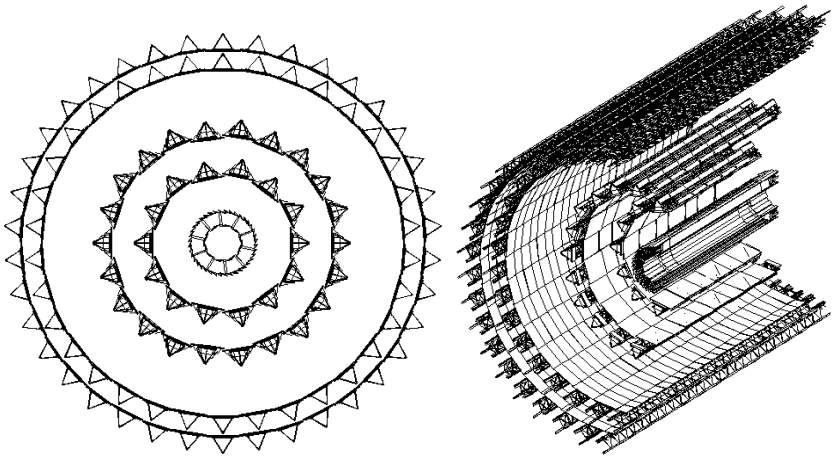

Fig. 1. Front view and axonometric-cut view of the ITS as described in the simulation program.

cabling and cooling connections for all the ITS and include the appropriate mechanical links to the TPC and to the SPD layers. The latter are assembled in two half-cylinder structures, specifically designed for safe installation around the beam pipe.

The large number of channels in the ITS layers are readout via aluminium–Upilex microcables [9] whose low thickness (e.g. 12 μm Upilex + 14 μm Al for signal lines) keeps the material budget low. This cabling technology is used for both the signal and the power (high and low voltage) lines. A special development is in progress for the SDDs which need power lines at 2.4 kV. The thermal stress originating in the front–end hybrids and cooling system is not transferred to the detector thanks to the decoupling provided by these flexible microcables.

All the ITS front–end electronics is made up of ASICs which are remotely testable and programmable via a JTAG interface [10]. They are (or are being) implemented in a commercial 0.25 μm CMOS technology, using radiation-tolerant layout techniques developed at CERN [11]. A multi-level buffering to derandomize the event arrival times, and reduce the needs of readout-bandwidth, is present in the readout schemes of the SPD, SDD and SSD. All the ITS ladders have some electronics placed at their extremities. It is devoted to detector-specific fine voltage regulation, readout control, detector-specific zero-suppression, and interfacing with three external systems: the data acquisition, the trigger and the slow detector control. Digital optical links are used for the first two systems.

Particular care was taken in the design of the cooling system and of the temperature monitoring; indeed the SDDs and the TPC are sensitive to temperature variations in the 0.1 K range. A leakless water cooling system at room temperature is the chosen solution for all ITS layers, but the use of other liquid

coolants is still being considered. For the temperature monitoring dedicated integrated circuits are mounted on the readout boards and specific calibration devices are incorporated in the SDDs. The front–end electronics for the SDDs and SSDs are mounted on rigid heat–exchanging hybrids, clipped onto thin–walled (70 μm thick) stainless-steel cooling pipes running along the ladder structure.

3.1 The Silicon Pixel Detectors (SPD)

The ALICE SPD modules each consist of a 256 (Rφ) $\times$ 160 (z) cells detector matrix, flip-chip bonded to 5 front–end chips. The detector and the electronics are, respectively, 150 μm and 100 μm thick. Four modules are aligned in the z direction to form a ladder, and a group of six ladders from the two layers constitutes one of the ten angular sectors of the SPD barrel.

Each front-end chip [12] contains the readout channels of 256 (Rφ) $\times$ 32 (z) detector cells. The pixel signal feeds a preamplifier-shaper with leakage current compensation, which is followed by a discriminator with individually tunable threshold. The discriminator output is sampled at 40 MHz and, after a delay line, it is strobed by the Level–1 trigger (L1, latency of 5.5 μs) into a 1-bit 4-level-deep FIFO buffer. On the Level–2 trigger, (L2, latency of 100 μs) the FIFO output is sent to the pilot chip at the end of the ladder, for the zero–suppression and data formatting, and then, through an optical link, to a remote router which multiplexes several ladders and feeds the DAQ. The dead time introduced by the readout of the SPD is estimated to be below 10% in the worst case, corresponding to ALICE running with Ca–Ca beams at high luminosity, with an L1 rate of 2.5 kHz.

The SPD barrel can determine the z-coordinate of the primary vertex by correlating the hits of the inner layer with all the hits in the second layer within a chosen azimuthal-angle window centered on the first hit. Choosing a narrow azimuthal window lowers the combinatorial background and selects the hits belonging to higher-momentum tracks, which are less influenced by multiple scattering. On the other hand, a too tight window could diminish too much the number of correct combinations. The azimuthal range accepted has therefore to be optimized for each particle density. The precision of such a measurement as a function of the charged particle density $\mathrm{d}N_{\mathrm{ch}}/\mathrm{d}\eta$ can be parametrized as $\sigma_z = 7\ \mu\mathrm{m} + 260\ \mu\mathrm{m}/\sqrt{\mathrm{d}N_{\mathrm{ch}}/\mathrm{d}\eta}$. The additive constant represents the influence of the ITS residual misalignment. At the typical particle densities of the pp collisions the precision is limited by statistics, and the track parameter resolution at the vertex is determined by multiple scattering and coordinate measurement errors. At the particle densities of the central Pb–Pb collisions the precision is determined by residual misalignment and not by statistics.

The other two coordinates of the primary vertex are fixed by the small size of the LHC bunch, which has a r.m.s. width of $\sigma_{\rm x} = \sigma_{\rm y} = 15$ μm.

3.2 The Silicon Drift Detectors (SDD)

The ALICE SDD final prototypes were produced by Canberra Semiconductor, Belgium, on 300 μm thick 5" NTD wafers with a resistivity of 3 kΩcm. Their active area is split into two adjacent 35 mm long drift regions, each equipped with 256 collecting anodes, with built-in voltage dividers for the drift and the guard regions and with three rows of point-like MOS charge injectors to allow the drift velocity monitoring. A careful design of the cathode strips prevents any punch-through which would deteriorate the voltage divider linearity. The drift velocity is orthogonal to the beam axis and therefore to the magnetic field, but the (weak) Lorentz force is compensated by the confining electric drift field; hence there are essentially no effects on the charge transport. Beam tests with minimum ionizing particle (MIPs) have shown that a drift field of about 670 V/cm, corresponding to a maximum drift time of 4.3 μs, ensures a good trade-off between signal–to–noise ratio and sufficient charge spreading among adjacent anodes [13].

The SDD front-end electronics [14] consists of two integrated circuits. The first one, named PASCAL, amplifies the signals from 64 anodes and stores them in analogue ring memories of 256 steps at 40 MHz rate. The preamplifiers feature a dynamic range of 32 fC (8 MIPs), leakage current compensation, and a shaping time of 38 ns. On the L1 trigger, PASCAL freezes the memories and digitizes their contents by means of 10-bit successive approximation A/D converters at about 3 Msample/s. The data are written in one of the two digital buffers made available by the second ASIC, called AMBRA, which derandomizes the events. It also implements a 10-bit to 8-bit data compression which keeps the percentage quantization error almost constant. The L2 trigger enables the data transfer at 40 MHz from the AMBRAs to the end–ladder modules, where a third ASIC performs the zero-suppression, the data compression [14,15] and transmits the results to the DAQ system.

Several SDD prototypes have been tested with MIPs at the CERN-SPS. The resolution along the drift direction has a mean value of 35 μm. After the correction of systematic errors due to dopant concentration inhomogeneities, observed both in beam tests and in the laboratory with a laser beam [16], the resolution along the anode direction has values better than 30 μm over 90% of the whole drift path. At drift fields greater than 580 V/cm the detection efficiency is essentially 100% [13].

The monitoring of the drift velocity is performed by measuring the drift time of

the MOS injectors [17,18]. It has been proven in a beam test environment that the temperature dependence of the drift velocity ($v \propto T^{-2.4}$) can be measured with an accuracy of about 0.1 %, corresponding to temperature variations of the order of 0.1 K [19].

3.3 The Silicon Strip Detectors (SSD)

The two outer layers of the ITS consist of double-sided SSDs with 400 mm long strips, 36 mrad stereo angle between the strips of the two sides, punch-through biasing, integrated decoupling capacitors and p-spray isolation on the ohmic side. The stereo angle value is a trade-off between the resolution along the z axis and the number of residual ghost hits after exploiting the correlation of the charges read out on the two detector sides. At the highest expected particle density the charge matching increases the fraction of unambiguous hits from 60 % to 96 %. The detectors are mounted with the strips nearly parallel to the beam axis; their stereo angles are +9 mrad on one detector side and -27 mrad on the other; the detectors of one layer are mounted upside-down with respect to those of the other layer. The resulting 4-axes system reduces by about 40 % the number of hit candidates for a track.

The SSD electronics consists of three major parts: the front-end chips, the end-cap electronics and the front-end readout modules (FEROMs). Each detector is served by twelve A128C front-end chips [20,21]. These contain 128 preamplifier-shaper circuits followed by sample-hold circuits. Their main features are: tunable shaping time of $1.4 \div 2\mu$s, noise figure of 400 e, dynamic range of 13 MIP and power dissipation of only 340 μW per channel, which allows a minimal cooling system. The readout is made at a rate of 10 Mhz through a 128:1 serial multiplexer. The A128C has been produced and tested for its functionality and its behaviour in a radiation environment. As expected from the simulations, it has a non-linearity of 1 % in the range $\pm$10 MIP and below 4 % in the full range. With the low radiation levels expected at the two outer layers of the ITS the radiation damage will be negligible, but protection against latch-up will be necessary. Therefore the A128C is being implemented in the same technology adopted for the SPD and SDD front–end electronics.

The FEROMs are located approximately 5 m far from the end-cap electronics. On the L1 trigger, they initiate the readout of the front–end chips, the 10-bit digitization for several half-ladders in parallel, and the local buffering of the data. The digitization completes within 160 μs. On the L2 trigger, they transmit the data to the DAQ system.

Both detailed simulations and beam tests of the detector have been performed. Several detector prototypes have been produced by Canberra and Eurysis.

They have shown satisfactory performance and radiation hardness. In particular: the measured S/N ratio is greater than 40, the spread of the charge matching distribution has $\sigma(Q_{\rm p-side} - Q_{\rm n-side}) = 6.1\%$; the precisions in the Rφ and Rz planes are 15 μm and 730 μm respectively.

4 ITS performances

The track finding for the system TPC and ITS is based on the Kalman filter algorithm [22], widely used for high-energy physics detectors. It starts from track–seed finding in the outermost pad rows of the TPC. Then it proceeds with the Kalman filter through all the TPC, starting with the stiffest tracks, as found from the seeds, removing the assigned clusters, and continuing with the softer tracks. When matching the track from the TPC with the ITS hits, the described procedure is unreliable due to the distance between the two detectors and to the high hit density in the ITS. Therefore two improvements to the filter have been implemented. First, a loose primary vertex information, derived from the SPD, is used, assuming $\sigma_{\rm z} = 1.0$ mm and $\sigma_{\rm xy} = 0.1$ mm. This allows to find tracks from secondary vertices close to the primary one in a single tracking pass. Second, for each TPC track, a tree of ITS hit candidates having reasonable χ^2 is built. Then the path along the tree is chosen which, for the maximum number of hits, gives the minimum sum of the χ^2.

The efficiency of the TPC reconstruction using the fast simulation is close to 100%, normalized to the so–called "findable" tracks (tracks which cross at least 40% of all TPC pad rows and produce at least one hit in the rows chosen for the seed-finding procedure). Therefore the performances reported below, have to be interpreted as the performance of the matching between the TPC and the ITS, and of the ITS tracking itself. In the track–finding in the ITS, we call "good tracks" those for which at least five of the six generated hits have been correctly assigned; instead, if one of the generated hits is assigned to the wrong track, that one is called a "fake track". Moreover, because we assume a detection efficiency of 98% for the pixel layers and 95% for the other ITS layers, the maximal achievable ITS track–finding efficiency is 94.5%. The simulations show a total ITS track-finding efficiency between 85% and 95% depending on $p_{\rm T}$. The fake-track probability is below 5% except for $p_{\rm T}$ in the range 100–200 MeV/c where it increases to 10%. These results are consistent with the large influence of multiple scattering at low momenta.

After tracking with the system TPC–ITS, all the assigned hits are removed from the ITS, and the low-momentum tracks ($p_{\rm T} \leq 100$ MeV/c) are searched for using a neural network algorithm. This looks only for pions and electrons because kaons and protons threshold momenta to pass through the ITS material are 120 MeV/c and 180 MeV/c, respectively. We achieve an efficiency

of 70% and higher for electrons with p_{T} above 30 MeV/c, and for pions with p_{T} above 60 MeV/c.

The relative momentum resolution for pions with p_{T} in the range 0.2–2.0 GeV/c varies between 1.35% and 1.7% (fig. 2). The angular resolution, with the vertex constraint and in the heavy ion case, ranges from 1.7 mrad to 0.4 mrad in the same transverse momentum interval, being sufficient for particle interferometry. For the p-p case these values become 2.6 and 0.6 mrad respectively. Without vertex constraint, the angular resolutions worsen by about 8%. This is clearly the effect of the 1mm thick beryllium beam pipe. For the same reason, we see a degradation in the impact parameter resolution of about 11% for the transverse projection, which is the most precise one. With the vertex constraint, it varies from 300 μm to 40 μm for kaon p_{T} in the interval 0.3–2.0 GeV/c (fig. 3). The momentum precision, using only the ITS, will be worse than 9% at the nominal magnetic field ($B = 0.2$ T) and slightly better than 5% at the doubled value of the field, compared to 1.35% in the standard case. The TPC stand-alone will have a momentum resolution of around 1.5% at this transverse momentum, but at larger p_{T} its momentum precision deteriorates very rapidly, as shown in fig. 2.

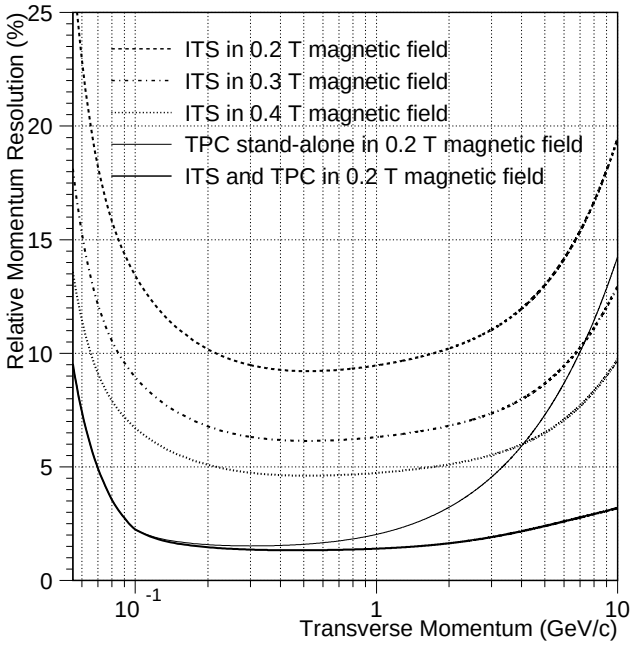

Fig. 2. Relative momentum resolution for pions using only the ITS in the nominal magnetic field ($B = 0.2$ T) and higher fields, compared with the resolution using both ITS and TPC, and TPC stand-alone in the nominal magnetic field.

For the $\mathrm{d}E/\mathrm{d}x$ determination only tracks having at least three points, which do not overlap with other hits, are used. This gives a factor of 0.9 in the efficiency for central Pb–Pb collisions. Then the specific energy loss is calculated as the mean value of the lowest two out of the four or three measurements. This well–known procedure provides a $\mathrm{d}E/\mathrm{d}x$ distribution with a Gaussian form

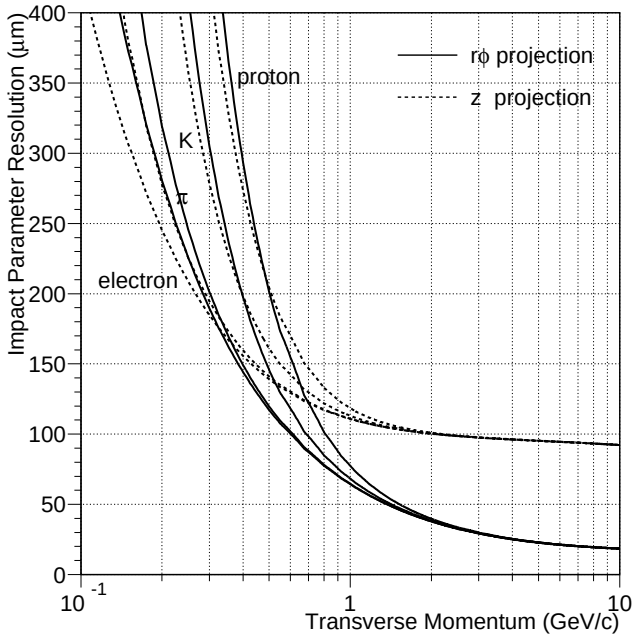

Fig. 3. Resolution for the distance of the closest approach between the track and primary vertex (impact parameter) imposing the primary vertex constraint.

and r.m.s. of 9–11%, depending on the momentum and particle type. For the electron/pion separation we use a momentum-dependent cut on the value of the truncated mean. We can identify the electrons with an efficiency of 70% and higher, with a 10% contamination by pions, for momenta up to 160 MeV/c. By changing the value of the cut we can always increase the efficiency if we accept higher contamination, and vice versa. For hadron identification we use again a momentum-dependent cut, up to a certain momentum (410 MeV/c for π/K separation and 730 MeV/c for K/p separation) where the species can be well separated. From this value up to the maximal momentum (530 MeV/c for π/K separation and 1030 MeV/c for K/p separation) we calculate the weights [23] that provide a statistical separation, still usable in event–by–event studies. We have achieved effective identification of kaons with a total contamination of about 2% in the momentum range 150–530 MeV/c, and of protons with a total contamination of about 6% in the momentum range 200–1030 MeV/c.

The precision in the particle correlation study is determined by the momentum resolution. It will be possible to study the shape of the correlation function up to radii of 30–40 fm for different particle species. The single-event study is also affected by the particle density and by the track-finding efficiency. With the lower tracking efficiency of the detailed simulations and the highest particle density, a relative error of about 22% can be achieved for the effective sizes of 15 fm in single-event pion interferometry,

We have estimated the yields of reconstructed hyperons, assuming the highest particle density and production rates per pion of 5%, 2%, 0.5% and 0.05%

respectively for K^0_S, Λ, Ξ^- and Ω^-. The reconstruction efficiencies for K^0_S and Λ are of about 50%, and for the cascade decays of Ξ^- and Ω^- they exceed 30%. Under these assumptions, around 50 K^0_S will be detected in one Pb–Pb central event. This will allow us to study the fluctuation of the K^0_S multiplicity on an event-by-event basis with a precision of about 15%. The estimated yields per central Pb–Pb event for the other hyperons are: 6.6 for Λ, and about 0.1 and 0.01 for Ξ^- and Ω^-, respectively.

The most promising decay channel for open charm detection is the $D^0 \to K^-\pi^+$ decay, having branching ratio 3.9% and $c\tau$ 124.4 μm. The lowest estimate for charm production implies, for the ALICE detector, 0.55 D^0 or $\overline{D^0}$ decays into the charged $K\pi$ channel with both decay products in the acceptance. For the combinatorial background we have used the highest multiplicity. The estimated significance of D^0 detection resulted to be $S/\sqrt{(B)} = 20$ for 10^7 central Pb-Pb events. For the case of D^+ the the value $S/\sqrt{(B)} = 6.5$ was obtained. The significance increases proportionally to the charm production rate. For lower particle densities the significance increases linearly in the case of the D^0 meson, and as a power $-3/2$ of the density for the D^+ meson.

References

[1] N. Antoniou *et al.*, Letter of Intent for A Large Ion Collider Experiment, CERN/LHCC/93–16 (1993).

[2] ALICE Collaboration, Technical Proposal, CERN/LHCC/95–71.

[3] ALICE Collaboration, ALICE TP addendum 1, CERN/LHCC/96-32

[4] ALICE Collaboration, ALICE ITS Technical Design Report, CERN/LHCC/99-12

[5] ALICE Collaboration, ALICE TP addendum 2, CERN/LHCC/99-13

[6] X. N. Wang and M. Gyulassy, Phys. Rev. D44 (1991) 3501.

[7] A. Fassò *et al.*, Nucl. Instr. and Meth. A395 (1993) 459.

[8] R. Brun *et al.*, CERN program library W5013.

[9] De Haas *et al.*, *Proceedings 5th Conference on Electronics for LHC Experiments* (Snowmass, CO, USA, 1999) Ed. by C. Decosse, CERN, Geneva, 1999; CERN-99-09, CERN-LHCC-99-033, p.143.

[10] IEEE Standard Test Access Port and Boundary-Scan Architecture (IEEE Std 1149.1)

[11] M. Campbell, "An Introduction to Submicron Electronics", Proceedings of this conference, and references therein.

[12] P. Chochula, "The ALICE Pixel Chip", Proceedings of this conference, and references therein.

[13] D. Nouais *et al.*, Nucl. Phys. Proc. Suppl. B78 (1999) 252.

[14] G. Mazza *et al.*, Nucl. Phys. A661 (1999) 694c.

[15] G. Alberici *et al.*, "Image Compression for the Silicon Drift Detectors in the ALICE Experiment", *Proceedings International Conference on Imaging Techniques in Particle Physics, Nuclear Physics, Astrophysics, Medicine and Biology* (Stockholm, Sweden, 2000), Nucl. Instr. and Meth. A in press.

[16] D. Nouais *et al.*, "Spatial Accuracy of $70 \times 75mm^2$ Silicon Drift Detectors Accounting for Dopant Concentration Fluctuations", *Proceedings 8th Pisa Meeting on advanced detectors* (La Biodola, Isola d' Elba, Italy, 2000), Nucl. Instr. and Meth. A in press; and http://documents.cern.ch/archive/electronic/cern/preprints/ali/ali-2000-002.pdf .

[17] V. Bonvicini *et al.*, Il Nuovo Cim. A112 (1999) 137.

[18] V. Bonvicini *et al.*, Nucl. Instr. and Meth. A439 (2000) 476.

[19] D. Nouais *et al.*, Nucl. Instr. and Meth. A450 (2000) 388.

[20] L. Hébrard *et al.*, A128C: A CMOS Full Custom ASIC for the Readout of Silicon Strip Detectors in the ALICE Experiment, Proc. of the Third Workshop on Electronics for LHC experiments, Imperial College, London, September 22–26, 1997, pp. 173–177.

[21] L. Hébrard, J.P. Blondé, C. Colledani, G. Clauss, 'Design and Test of a CMOS Low-Power Mixed-Analog/Digital ASIC for Radiation Detector Readout Front Ends, Proc. of the 11th Annual IEEE International ASIC Conference, ASIC'98, Rochester, New York, September 13–16, 1998.

[22] B. Batyunya, Yu. Belikov, K. Šafařík, Internal Note ALICE 97-24 (1997), and references therein.

[23] B. Batyunya, Internal Note ALICE 98-49 (1998).